Absence of magnetic order and emergence of unconventional fluctuations in the $J_{\text{eff}} = \frac{1}{2}$ triangular-lattice antiferromagnet $YbBO_3$

K. Somesh,[1] S. S. Islam,[1] S. Mohanty,[1] G. Simutis,[2,3,*] Z. Guguchia,[4] Ch. Wang,[4] J. Sichelschmidt,[5] M. Baenitz,[5] and R. Nath[1,†]

[1]*School of Physics, Indian Institute of Science Education and Research Thiruvananthapuram, Kerala 695551, India*
[2]*Laboratory for Neutron and Muon Instrumentation, Paul Scherrer Institut, CH-5232 Villigen PSI, Switzerland*
[3]*Department of Physics, Chalmers University of Technology, SE-41296 Göteborg, Sweden*
[4]*Laboratory for Muon Spin Spectroscopy, Paul Scherrer Institut, Villigen PSI, Switzerland*
[5]*Max Planck Institute for Chemical Physics of Solids, Nöthnitzer Strasse 40, 01187 Dresden, Germany*

(Received 28 September 2022; revised 3 February 2023; accepted 3 February 2023; published 21 February 2023)

We present the ground state properties of a new quantum antiferromagnet, $YbBO_3$, in which the isotropic Yb^{3+} triangular layers are separated by a nonmagnetic layer of partially occupied B and O(2) sites. The magnetization and heat capacity data establish a spin-orbit entangled effective spin $J_{\text{eff}} = \frac{1}{2}$ state of Yb^{3+} ions at low temperatures, interacting antiferromagnetically with an intralayer coupling $J/k_B \simeq 0.53$ K. The absence of oscillations and a 1/3 tail in the zero-field muon asymmetries rules out the onset of magnetic long-range order as well as spin freezing down to 20 mK. An anomalous broad maximum in the temperature-dependent heat capacity with an unusually reduced value and a broad anomaly in the zero-field muon depolarization rate centered at $T^* \simeq 0.7J/k_B$ provide compelling evidence for a wide fluctuating regime ($0.2 \lesssim T/J \leqslant 1.5$) with slow relaxation. We infer that the fluctuating regime is a universal feature of highly frustrated triangular-lattice antiferromagnets while the absence of magnetic long-range order is due to perfect two-dimensionality of the spin lattice protected by nonmagnetic site disorder.

DOI: 10.1103/PhysRevB.107.064421

I. INTRODUCTION

Frustrated magnets are a special class of systems where the ground state degeneracy leads to captivating low-temperature properties. One such emergent phenomenon is the quantum spin liquid (QSL), a disordered state characterized by fractionalized excitations, quantum entanglement, and the absence of magnetic long-range order (LRO) [1]. The quest for this exotic phase has escalated remarkably since Anderson's proposal of the resonating valence bond model, a prototype of the QSL in spin-$\frac{1}{2}$ triangular-lattice antiferromagnets (TLAFMs) [2]. However, subsequent theoretical studies revealed three-sublattice Néel order as the real ground state for Heisenberg TLAFMs [3]. From a pragmatic point of view, the real materials are often plagued with a certain degree of perturbations such as exchange anisotropy, couplings beyond nearest neighbor (NN), structural disorder, etc., that may alter the actual ground state and pave the way for even richer physics [4–7]. A prominent manifestation of such effects is the broad fluctuating regime with slow dynamics observed in TLAFMs $(Na, K, H)CrO_2$ in low temperatures [8,9]. Indeed, spin-$\frac{1}{2}$ TLAFMs with the above perturbations have recently been perceived as an ideal host for a gapped or gapless QSL and other exotic phases [10,11].

Rare-earth-($4f$)-based TLAFMs, mainly with ytterbium (Yb^{3+}), set a new platform to explore nontrivial phases of matter. Here, the interplay of strong spin-orbit coupling (SOC) and a noncubic crystal electric field (CEF) leads to a Kramers doublet with an effective $J_{\text{eff}} = \frac{1}{2}$ ground state. Moreover, the strong SOC is expected to induce anisotropic exchange interactions, which is proposed to be an ingredient in stabilizing the QSL state [12]. Furthermore, disorder in the frustrated magnets is believed to destroy the states that are stabilized in disorder-free compounds and concedes various fascinating ground states [13]. For instance, recently, it was found that structural disorder can trigger bond randomness and promote QSL-like states [4,5]. The most celebrated compounds in this category are $Yb(Mg, Zn)GaO_4$, where disorder due to site mixing of Ga^{3+} and Mg^{2+} or Zn^{2+} leads to randomized interactions, which apparently forbids LRO and results in highly fluctuating moments [14–20]. This opens up a new paradigm for realizing randomness-induced nontrivial states that mimic QSLs [21–24]. The disorder-free chalcogenides $(Na, Cs, Li)YbX_2$ (X = O, S, and Se) featuring a triangular lattice also show the signature of a QSL in zero field and field-induced transition in higher fields [25–32]. Though no LRO is detected down to 50 mK in another disorder-free TLAFM, $Ba_3Yb(BO_3)_3$, the dominant interaction is found to be long-range dipole-dipole coupling rather than exchange interactions [33–35].

Herein, we report a comprehensive study of a new TLAFM, $YbBO_3$, with partial nonmagnetic site disorder. It belongs to the vaterite family having the general formula

*gediminas.simutis@psi.ch
†rnath@iisertvm.ac.in

 ©2023 American Physical Society

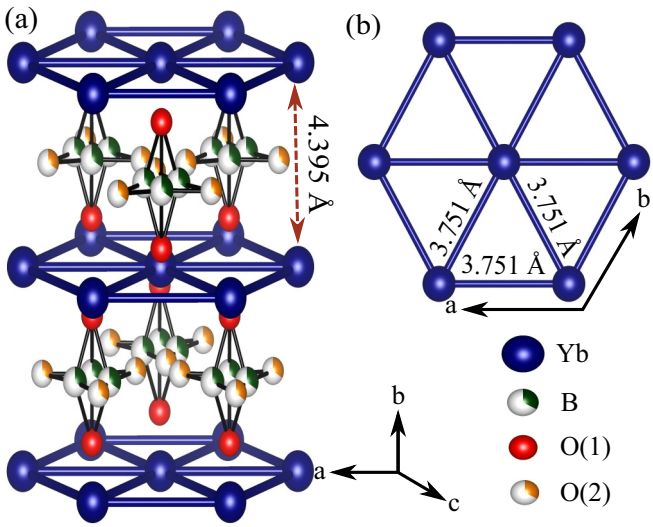

FIG. 1. (a) Crystal structure of $YbBO_3$ showing triangular Yb^{3+} sheets separated by a layer of B and O atoms. The O(1) site is fully occupied while O(2) and B sites are each only 33% occupied. (b) A section of the Yb^{3+} layer with equilateral triangles.

RBO_3 (R = rare earth) with the hexagonal crystal structure of space group $P6_3/m$ (No. 176) [36,37]. The magnetic Yb^{3+} ions fully occupy the regular triangular sites and are free from any sort of magnetic site disorder (see Fig. 1) [36]. One of the two oxygen sites [O(2)] and the boron site are each 33% occupied. The triangular layers are separated by a layer of these partially occupied B and O(2) sites. Figure 1(b) presents the in-plane structure of the Yb^{3+} forming triangular units with nearest-neighbor (NN) distance 3.751 Å. The ratio of interplane distance to intraplane distance ($d_{\text{inter}}/d_{\text{intra}}$) between Yb^{3+} ions is ∼1.17. We choose $YbBO_3$ in order to investigate how the nonmagnetic site disorder affects the local environment of Yb^{3+} and hence the ground state. We illustrate that the Yb^{3+} ions form a Kramers doublet with effective spin $J_{\text{eff}} = \frac{1}{2}$ at low temperatures. Despite a relatively large Curie-Weiss temperature $\theta_{\text{CW}} \simeq -0.8$ K, magnetic LRO is forbidden down to 20 mK. Intriguingly, the muon spin relaxation (μSR) measurements reveal a broad low-temperature fluctuating regime with slow dynamics. These features are attributed to the combined effects of magnetic frustration and nonmagnetic site disorder.

II. EXPERIMENTAL DETAILS

A polycrystalline sample of $YbBO_3$ was synthesized via the conventional solid-state reaction technique. A stoichiometric mixture of the high-purity reactants Yb_2O_3 (99.99%) and H_3BO_3 (99.99%) (15% excess H_3BO_3 is taken to compensate for the loss of B during the heating process due to the volatile nature of H_3BO_3) was ground and preheated at 500 °C to decompose H_3BO_3 into B_2O_3, followed by a firing at 900 °C with an intermediate grinding. The phase purity and crystal structure (hexagonal, $P6_3/m$) of the compound were confirmed by powder x-ray diffraction (XRD) measurements using a PANalytical x-ray diffractometer (Cu K_α radiation, $\lambda_{\text{av}} \simeq 1.541\,82$ Å). The temperature-dependent powder XRD measurements were performed over the temperature range 15 K $\leqslant T \leqslant$ 300 K using a low-temperature attachment (Oxford PheniX) to the diffractometer. Magnetization M was measured as a function of temperature T and applied field H using a superconducting quantum interference device (SQUID) magnetometer (MPMS-3; Quantum Design). Measurements down to 0.4 K were carried out using a ^{3}He (iHelium3; Quantum Design Japan) attachment to the MPMS. Heat capacity [$C_p(T)$] measurement was performed on a small piece of sintered pellet using the relaxation technique in the physical property measurement system (PPMS; Quantum Design). For measurements down to 0.4 K, a ^{3}He attachment was used in the PPMS.

We measured electron spin resonance (ESR) on the polycrystalline $YbBO_3$ sample using a standard continuous-wave ESR setup at X-band frequency (9.4 GHz). The temperature was varied between 3 and 295 K with a He-flow cryostat. ESR can be detected by the absorbed power P of a transversal magnetic microwave field as a function of a static external magnetic field $\mu_0 H$. To improve the signal-to-noise ratio, we used a lock-in technique by modulating the static field, which yields the derivative of the resonance signal dP/dH. The measured ESR spectra were fitted with a Lorentzian function including the influence of the counter-rotating component of the linearly polarized microwave field [38]. From the fit, we obtained the linewidth ΔH and the resonance field H_{res}, which determines the ESR g factor $g = h\nu/\mu_B H_{\text{res}}$. The ESR intensity I_{ESR} is a measure of the local static susceptibility of the probed ESR spins, i.e., in our case the local susceptibility of the Yb^{3+} spins [39]. We calculated $I_{\text{ESR}} \approx \text{Amp} \cdot \Delta H^2$, which approximates the integrated ESR absorption [26].

The muon spin relaxation (μSR) measurements were performed at the Swiss Muon Source (SμS) at Paul Scherrer Institute using a combination of two spectrometers [General Purpose Surface-Muon Instrument (GPS) and High-Field and Low Temperature Instrument (HAL)] down to 20 mK in zero field. The high-temperature measurements (1.5–50 K) were performed using the low-background high-throughput instrument, GPS [40]. The low-temperature data points were acquired using the zero-field option of the HAL spectrometer which allowed achieving temperatures as low as 20 mK. An overlapping temperature region was studied using both spectrometers to account for different sample holders and the fact that for the HAL measurement a pellet was made out of powder and mixed with GE varnish for structural stability and to ensure thermal contact.

III. RESULTS AND DISCUSSION

A. X-ray diffraction

Powder XRD data were collected at various temperatures. Rietveld refinement of the XRD data was carried out using the FULLPROF software package [41] that confirms the formation of a good-quality and pure-phase sample. Figures 2(a) and 2(b) depict the data at the two end temperatures. All the peaks could be appropriately indexed using the space group $P6_3/m$, and the obtained lattice parameters at room temperature [$a = b = 3.7344(1)$ Å, $c = 8.7433(1)$ Å, and $V_{\text{cell}} \simeq 105.59(1)$] are fairly comparable with previous reports

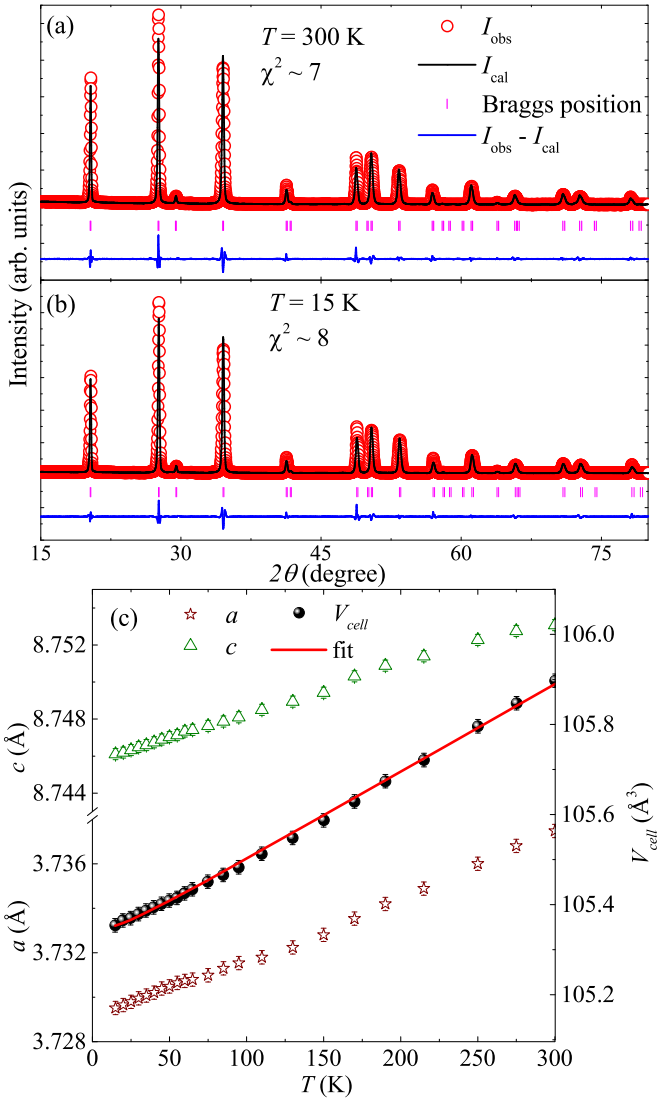

FIG. 2. Powder XRD data measured at (a) $T = 300$ K and (b) $T = 15$ K. The red solid line represents the Rietveld fit of the data. The Bragg positions are indicated by pink vertical bars, and the solid blue line at the bottom denotes the difference between the experimental and calculated intensities. (c) The variation of the lattice parameters (a, c, and $V_{\rm cell}$) as a function of temperature. The solid line denotes the fit of $V_{\rm cell}(T)$ by Eq. (1).

[36,37]. The atomic coordinates of different elements after refinement are given in Table I. Figure 2(c) presents the variation of lattice parameters over the temperature range 15–300 K. Upon cooling to 15 K, the parameters decrease monotonically. The temperature variation of unit cell volume $V_{\rm cell}$ was fitted by the equation [42]

$$V(T) = \gamma U(T)/K_0 + V_0, \tag{1}$$

where V_0 is the cell volume at $T = 0$ K, K_0 is the bulk modulus, and γ is the Grüneisen parameter. $U(T)$ is the internal energy, which can be derived in terms of the Debye approximation as

$$U(T) = 9nk_{\rm B}T\left(\frac{T}{\theta_{\rm D}}\right)^3 \int_0^{\theta_{\rm D}/T} \frac{x^3}{e^x - 1}dx. \tag{2}$$

Here, n is the number of atoms in the unit cell, and $k_{\rm B}$ is the Boltzmann constant. Using this approximation [see Fig. 2(c)], the Debye temperature $\theta_{\rm D}$ and other parameters were estimated to be $\theta_{\rm D} \simeq 208$ K, $\gamma/K \simeq 1.83 \times 10^{-5}$ Pa^{-1}, and $V_0 \simeq 105.384$ Å^3.

TABLE I. The Wyckoff positions and the refined atomic coordinates (x, y, and z) for each atom at room temperature.

Atom	Site	x	y	z	Occupancy
O1	4f	0.667	0.333	0.107(7)	1
O2	6h	0.776(5)	−0.197(6)	0.25	0.333
B1	6h	0.575(7)	0.417(8)	0.25	0.333
Yb1	2b	0	0	0	1

B. Magnetization

The magnetic susceptibility χ ($\equiv M/H$) as a function of temperature in different applied fields is depicted in Fig. 3(a). $\chi(T)$ increases monotonically as the temperature is lowered without showing any signature of magnetic long-range order (LRO) down to 0.4 K, a possible fingerprint of a disordered ground state. Measurements in zero-field-cooled (ZFC) and field-cooled (FC) conditions show no bifurcation (not shown), suggesting the absence of a spin-glass (SG) transition or spin freezing. Above 150 K, the inverse susceptibility $(1/\chi)$ for $H = 0.01$ T could be fitted well by $\chi(T) = \chi_0 + \frac{C}{T-\theta_{\rm CW}}$, where χ_0 is the T-independent susceptibility and the second term is the Curie-Weiss (CW) law. The fit yields $\chi_0 \simeq 6.3 \times 10^{-4}$ cm^3/mol, a high-T effective moment $\mu_{\rm eff}^{\rm HT}$ ($=\sqrt{3k_{\rm B}C/N_{\rm A}}$, where C, $k_{\rm B}$, and $N_{\rm A}$ are the Curie constant, Boltzmann constant, and Avogadro's number, respectively) $\simeq 4.53\ \mu_{\rm B}$, and a high-T CW temperature $\theta_{\rm CW}^{\rm HT} \simeq -62.6$ K. This value of $\mu_{\rm eff}^{\rm HT}$ is in good agreement with the expected value of 4.54 $\mu_{\rm B}$ for Yb^{3+} ($J = 7/2$, $g = 8/7$) in the $^4f_{13}$ configuration.

$1/\chi$ is found to change the slope below 80 K and displays a perfect linear behavior [inset of Fig. 3(a)] after substraction of the Van Vleck susceptibility $\chi_{\rm VV} \simeq 3.32 \times 10^{-3}$ cm^3/mol, obtained from the M vs H analysis, discussed later. A CW fit below 50 K yields $\mu_{\rm eff} \simeq 3.2\ \mu_{\rm B}$ and $\theta_{\rm CW} \simeq -0.8$ K. This experimental $\mu_{\rm eff}$ value is reminiscent of an effective spin $J_{\rm eff} = \frac{1}{2}$ with an average $g \simeq 3.6$. Furthermore, this value of g is significantly larger than the free electron g value of 2.0 due to the spin-orbit coupling and is consistent with the one extracted from the ESR experiment ($g \simeq 3.4$). Typically, at low temperatures, the magnetic behavior of Yb^{3+}-based compounds is governed by the Kramers doublets ($m_J = \pm\frac{1}{2}$) triggered by the CEF. In this case, the low-lying ground state is described by an effective pseudo-spin $J_{\rm eff} = \frac{1}{2}$ Hamiltonian, and the higher-lying levels produce a sizable Van Vleck contribution ($\chi_{\rm VV}$), which is different from the high-T χ_0 [12,14,43]. Indeed, several Yb^{3+}-based compounds have witnessed a $J_{\rm eff} = \frac{1}{2}$ ground state [26,27,44]. The negative sign of $\theta_{\rm CW}$ indicates dominant antiferromagnetic (AFM) intraplane coupling. Taking the number of NN spins $z = 6$ for a TLAFM and the experimental value of $\theta_{\rm CW}$, the NN AFM

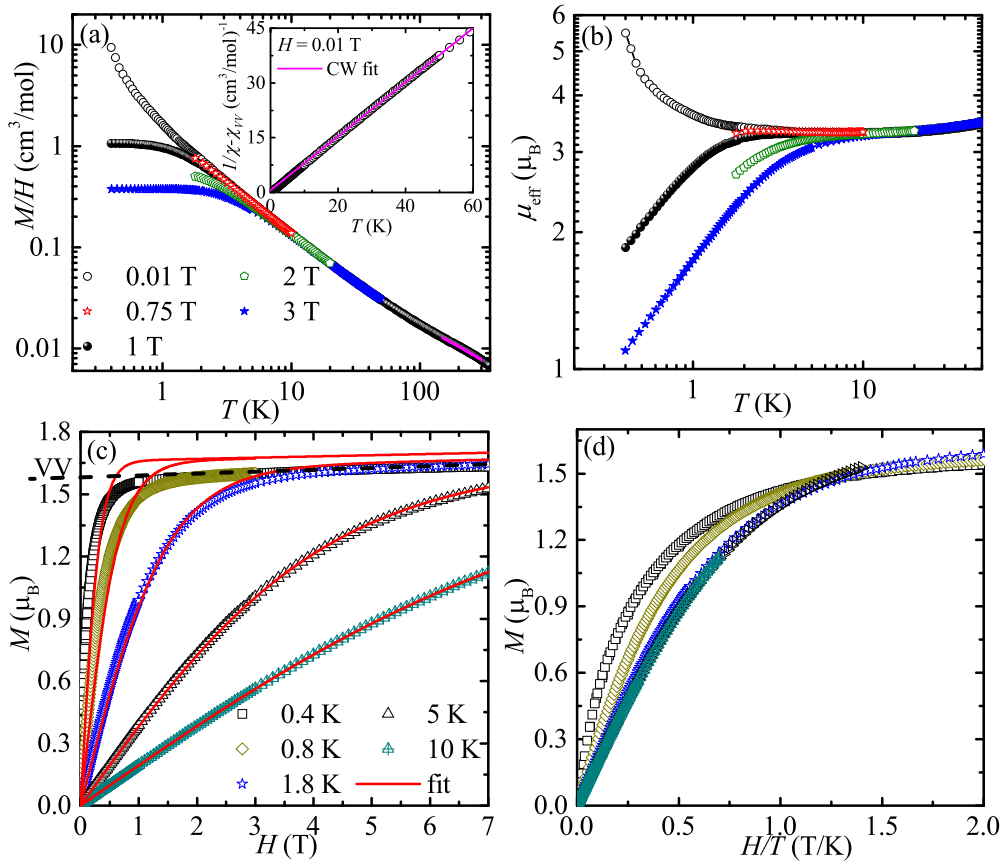

FIG. 3. (a) M/H vs T measured in various applied magnetic fields. Inset: The low-temperature $\chi(T)$ data (after subtracting χ_{VV}) along with the CW fit for $H = 0.01$ T. (b) μ_{eff} vs T. (c) M vs H measured at different temperatures along with the Brillouin fits. The horizontal dashed line marks the Van Vleck (VV) contribution. (d) M vs H/T to visualize the scaling of magnetization curves in the correlated regime.

exchange coupling [$\theta_{CW} = -zJS(S+1)/3k_B$] is estimated to be $J/k_B \simeq 0.53$ K.

In order to establish the correlated behavior at low temperatures, the effective magnetic moment μ_{eff} [$= \{(3k_B/N_A\mu_B^2)\chi T\}^{1/2} = 2.8284\sqrt{\chi T}$] vs T in different applied fields is plotted in Fig. 3(b). At high-Ts, μ_{eff} for all the fields approaches the free-ion value of ~4.53 μ_B and then falls to a plateau of ~3.3 μ_B in the T-range 4–20 K corresponding to $J_{eff} = \frac{1}{2}$. At low temperatures ($T < 4$ K), the curves deviate significantly from the plateau value, suggesting the growth of magnetic correlations. In a low field ($H = 0.01$ T), $\mu_{eff}(T)$ tends to show an upward curvature at low temperatures. This upward trend is a testimony of the presence of a weak ferromagnetic (FM) interaction along with the dominant AFM interactions [45,46].

Figure 3(c) presents the M vs H curves measured at various temperatures in the low-T regime. At $T = 0.4$ K, M saturates at around $H_S \simeq 0.7$ T and then increases weakly for higher fields due to the Van Vleck contribution. The value of H_S exactly reproduces the intraplane exchange coupling $J/k_B = g\mu_B H_S/4.5k_B \simeq 0.53$ K, taking $g \simeq 3.4$. This indicates that the interlayer and/or second-nearest-neighbor interactions are negligible and do not contribute to H_S [26]. The slope of the linear fit for $H > 3$ T results in $\chi_{VV} \simeq 3.32 \times 10^{-3}$ cm^3/mol, and the y-intercept corresponds to the saturation magnetization $M_{sat} \simeq 1.6\ \mu_B$. This value of M_{sat} provides $g \simeq 3.2$ for $J_{eff} = \frac{1}{2}$ ($M_{sat} = gJ_{eff}\ \mu_B$), which is close to the ESR value [26]. In the absence of exchange interaction, i.e., in the paramagnetic (PM) state, a magnetic isotherm can be modeled by $M(H) = \chi_{VV}H + gJ_{eff}N_A\mu_B B_{J_{eff}}(H)$, where $B_{J_{eff}}(H)$ is the Brillouin function for $J_{eff} = \frac{1}{2}$ [47]. Figure 3(c) presents the isotherm fits at different temperatures with fixed χ_{VV} that yield an average $g = 3.4(3)$, consistent with the ESR value. For $T > 1.8$ K, the isotherms are well fitted by the Brillouin function, which comprehends the uncorrelated spins. However, for $T \leqslant 1.8$ K, the fit deviates significantly from the experimental data reflecting the growth of magnetic correlations. It is also observed that in the low-field regime, there is a small enhancement of magnetization compared to the Brillouin fit, which further substantiates a weak FM correlation, stemming possibly from minute next-nearest-neighbor interactions. In order to visualize this striking feature, we scaled the x-axis dividing H by T and plotted the result in Fig. 3(d). Above 1.8 K, all the curves collapse on to a single curve, implying the PM nature of the spins, while below 1.8 K, the curves progressively deviate from the scaling, ascertaining the emergence of strong magnetic correlations.

C. Electron spin resonance

The electron spin resonance (ESR) signal for three temperature regimes is shown in Fig. 4(a). The most well-defined spectral shapes were detected in a temperature regime between 20 and 80 K with a corresponding g value of $g = 3.4(2)$

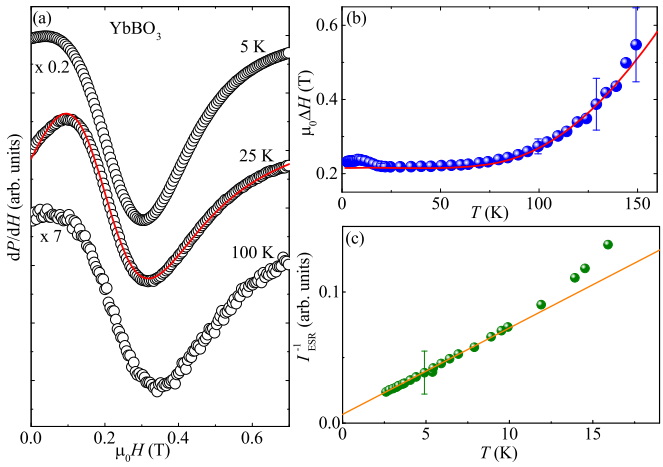

FIG. 4. (a) ESR spectra of $YbBO_3$ at three temperatures. The red solid line depicts a symmetric Lorentzian line shape with a g value of $g = 3.4(0)$. (b) ESR linewidth ΔH; the solid line refers at higher temperatures to a relaxation mechanism via the first excited crystalline electric field level of Yb^{3+} at $\Delta_{ESR}/k_B = (500 \pm 100)$ K. (c) Temperature dependence of the reciprocal ESR intensity (I_{ESR}^{-1}) and the solid line represents the linear behavior.

of a symmetric Lorentzian line, as indicated by the red solid line. The low-temperature CW fit of I_{ESR}^{-1} [see Fig. 4(c)] yields a small CW temperature ($\theta_{CW} \sim -1$ K) that is consistent with the uncertainties in the determination of I_{ESR}. The temperature dependence of the ESR linewidth ΔH is shown in Fig. 4(b). For temperatures above ~70 K, ΔH broadens according to $\Delta H \propto 1/\exp(\Delta_{ESR}/k_B T) - 1$ (red solid line). This behavior indicates a spin-lattice relaxation dominated by an Orbach process. Via spin-orbit coupling, this process involves a phonon absorption to and an emission from a crystalline electric field split electronic energy level Δ_{ESR} above the ground state [39,48]. We obtained $\Delta_{ESR}/k_B = (500 \pm 100)$ K. Towards low temperatures, the spectra display a moderate broadening, indicating the increasing influence of Yb^{3+} spin correlations.

D. Heat capacity

Heat capacity C_p measured as a function of temperature down to 0.4 K in different magnetic fields is shown in Fig. 5(a). At high temperatures, $C_p(T)$ is completely dominated by the phononic contribution (C_{ph}). Below about 4 K, C_p in zero field increases towards low temperatures as the magnetic correlation sets in and then levels off below ~0.55 K, similar to $NaYb(O, S)_2$ [25,26]. The absence of any sharp peak rules out the onset of magnetic LRO down to 0.4 K in zero field. An external magnetic field suppresses the magnetic correlation and gives rise to a broad anomaly which moves

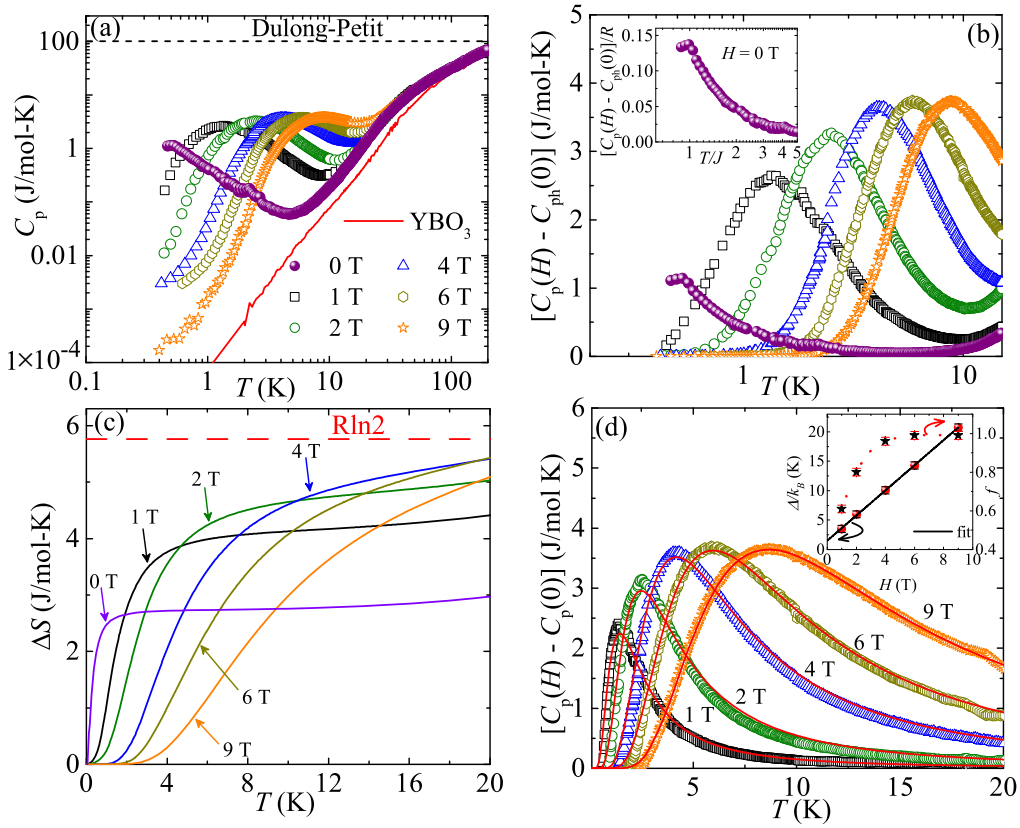

FIG. 5. (a) C_p vs T measured in different applied magnetic fields. The solid line represents C_{ph} vs T of the nonmagnetic analog YBO_3. The horizontal dashed line guides the Dulong-Petit value. (b) $C_p(H) - C_{ph}(0)$ vs T in different fields. Inset: $[C_p(H) - C_{ph}(0)]/R$ vs T/J in zero field. (c) Entropy change ΔS vs T for different magnetic fields, obtained by integrating $[C_p(H) - C_{ph}(0)]/T$. (d) Schottky contribution $[C_p(H) - C_p(0)]$ vs T along with the fit using Eq. (3). Inset: Δ/k_B and f vs H in the left and right y-axes, respectively. The solid line represents the straight line fit to $\Delta/k_B(H)$.

towards higher temperatures with field. This broad feature portrays the Schottky anomaly due to the Zeeman splitting of the ground state Kramers doublet. The magnetic heat capacity $C_{\rm mag}$ is obtained by subtracting the heat capacity ($C_{\rm ph}$) of the nonmagnetic analog YBO_3 from the total $C_{\rm p}$ of $YbBO_3$ [see Fig. 5(b)]. The change in magnetic entropy (ΔS) calculated by integrating $[C_{\rm p}(H) - C_{\rm ph}(0)]/T$ with respect to T is plotted in Fig. 5(c) for different magnetic fields. In zero field, ΔS attains a saturation value of ∼2.76 J/mol-K, which is almost 50% of $R \ln 2$, expected for $J_{\rm eff} = \frac{1}{2}$. This suggests that the remaining 50% entropy is released below 0.4 K due to the persistence of strong magnetic correlation. The saturation value of ΔS increases with H and is almost recovered to $R \ln 2$ above 2 T ($>H_{\rm S}$), expected for a two-level system.

To probe the Schottky contribution, the zero-field data $C_{\rm p}(0)$ are subtracted from the high-field data $C_{\rm p}(H)$ [i.e., $C_{\rm Sch}(T, H) = C_{\rm p}(H) - C_{\rm p}(0)$]. Figure 5(d) presents the fit of $C_{\rm p}(H) - C_{\rm p}(0)$ data using the two-level Schottky function [47]

$$C_{\rm Sch}(T) = fR\left(\frac{\Delta}{k_{\rm B}T}\right)^2 \frac{e^{(\Delta/k_{\rm B}T)}}{[1 + e^{(\Delta/k_{\rm B}T)}]^2}. \quad (3)$$

Here, f is the molar fraction of free spins, $\Delta/k_{\rm B}$ is the crystal field gap between the ground state and the first excited state doublets, and R is the gas constant. The estimated f and $\Delta/k_{\rm B}$ values are plotted as a function of H in the inset of Fig. 5(d). f increases with H and then saturates to a value of ∼1 for $H > 2$ T. This confirms that the magnetic field splits the energy levels and excites the free Yb^{3+} spins to the higher energy levels. For $H < H_{\rm S}$, a fraction of the spins are correlated, which is reduced with increasing field and above $H_{\rm S}$, all the free spins are excited. This explains why ΔS saturates to $R \ln 2$ and the peak maximum of the $C_{\rm p}(H) - C_{\rm p}(0)$ curves remains unchanged for $H > 2$ T [see Fig. 5(d)] [34]. In the inset of Fig. 5(d), $\Delta/k_{\rm B}$ increases linearly with H as expected, and a straight line fit results the zero-field energy gap $\Delta/k_{\rm B}(0) \simeq 1.5$ K, which possibly indicates an intrinsic field in the system [49]. From the value of $\Delta/k_{\rm B} \simeq 20.6$ K at 9 T, one can estimate the g value as $\Delta/k_{\rm B} = g\mu_{\rm B}H/k_{\rm B}$, which yields $g \simeq 3.3$, consistent with the ESR value.

Furthermore, $C_{\rm mag}$ ($= C_{\rm p} - C_{\rm ph}$) in zero field [inset of Fig. 5(b)] shows a plateau below 0.55 K with a maximum value $C_{\rm mag}^{\rm max}/R \simeq 0.137$. For a frustrated spin-$\frac{1}{2}$ TLAFM, one expects such a broad maximum at $T/J \simeq 0.84$ but with a reduced value $C_{\rm mag}/R \simeq 0.223$ [50] compared to a non-frustrated two-dimensional (2D) antiferromagnet (0.44) [51]. Though our maximum appears nearly at the anticipated position ($T/J \simeq 0.9$), the absolute value is significantly lower than that expected for a TLAFM. A similar peak-type feature in $YbMgGaO_4$ and $NaYbS_2$ is ascribed to disorder-induced and disorder-free QSLs, respectively [15,25]. In order to examine this peculiar feature, μSR experiments are carried out in zero field (ZF).

E. μSR

Muon spin is susceptible to extremely small magnetic field (∼10^{-5} T), and because of its much shorter time window (10 ns to 15 μs), μSR is an excellent probe for tracing the dynamics of slowly fluctuating magnets. In general, the

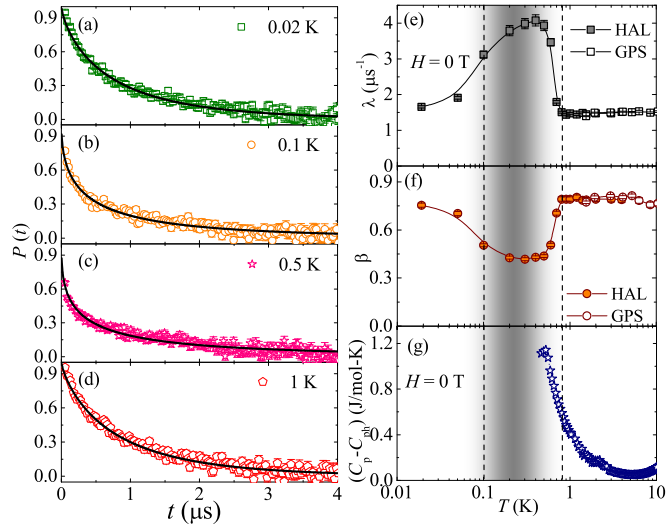

FIG. 6. (a)–(d) Normalized muon decay asymmetry as a function of time, with solid lines representing the fit using a stretched exponential function. Temperature dependence of (e) depolarization rate λ, (f) stretching parameter β, and (g) magnetic heat capacity. The shaded portion highlights the fluctuating regime.

ZF μ^+ spin depolarization rate λ is related to the spin-spin correlation function $\lambda_{\rm ZF} = \gamma_\mu^2 \int_0^\infty \langle B_{\rm loc}^\perp(t) \cdot B_{\rm loc}^\perp(0)\rangle\, dt \propto S_{\omega\to 0}^\perp$, where $S_{\omega\to 0}^\perp = \int_0^\infty \langle s_i^\perp(t) \cdot s_i^\perp(0)\rangle\, dt$ is the static spin structure factor [23,52]. Hence, by measuring muon asymmetry as a function of temperature, one can comprehend the correlated behavior of a spin system. Figures 6(a)–6(d) depict the muon asymmetry curves at different temperatures down to 20 mK, which are fitted well by a stretched exponential function, $P(t) = A(t)/A(0) = e^{-(\lambda t)^\beta}$. Here, $A(t)$ is the measured asymmetry and $A(0)$ is the instrument dependent initial asymmetry (approximately 0.118 and 0.213 for HAL and GPS, respectively). The introduction of stretching parameter β suggests that there is a distribution of the relaxation rates. The obtained λ and β along with $C_{\rm mag}$ ($= C_{\rm p} - C_{\rm ph}$) in zero field as a function of T are summarized in Fig. 6.

At high temperatures, the magnetic moments fluctuate very fast and only mildly depolarize the implanted muon before it decays, and the dominant depolarization channel is due to nuclear spins. This gives rise to a temperature-independent λ, as we observed in Fig. 6(e). Similarly, β remains temperature independent at high temperatures, and its value is slightly below 1 [see Fig. 6(f)], indicating a distribution likely due to weak disorder at the O site (muon stopping site) or a few muon sites. As the temperature is lowered below ∼0.8 K, which is close to $\theta_{\rm CW}$, β drops and λ increases rapidly exhibiting a broad minimum and maximum, respectively, centered at $T^* \simeq$ 0.4 K, which corresponds to the plateau position in $C_{\rm mag}$. The rapid increase in λ suggests the slowing down of fluctuating moments as the correlation sets in and replicates the behavior of $C_{\rm mag}(T)$. Upon further lowering the temperature, the values of β and λ recover back to their initial values below ∼0.1 K, clearly suggesting an exotic dynamical regime (0.1 K $\lesssim T \leqslant$ 0.8 K) with slow fluctuations, marked by shading in Figs. 6(e)–6(g) [53]. In the PM regime ($T > 1$ K), where $\lambda_{\rm ZF}$ is temperature independent, the spin fluctuation rate ν can be

calculated as $\nu = \sqrt{z}JS/\hbar \sim 8.542 \times 10^{10}$ Hz taking $z = 6$, $S = \frac{1}{2}$, and $J/k_B \simeq 0.53$ K [54,55]. In the fast-fluctuation limit, using the relation $\lambda_{ZF} = 2\Delta_\mu^2/\nu$, the distribution width of the local magnetic fields is estimated to be $\Delta_\mu \simeq 254$ MHz $\ll \nu$ considering λ_{ZF} ($T > 1$ K) $\simeq 1.5$ μs^{-1}.

IV. DISCUSSION

In the case of a conventional magnetic LRO, the muon decay asymmetry should exhibit an oscillating signal, while for a disordered, yet static case, such as a SG, if a powder sample is used, it should feature a nonoscillating and undamped 1/3 tail [23]. Furthermore, for a SG transition, β is expected to drop to ~0.33 as T tends to T_g, and λ is expected to show a peak or divergence [56–58]. The absence of any such signatures in Fig. 6 rules out both a static magnetic LRO and a SG transition. We also do not observe any saturation of the increased λ at low temperatures, in contrast to that reported for many QSL candidates due to persistent spin fluctuations [23,55,59]. Additionally, though the β value drops to ~0.4 at T^*, it recovers at low temperatures without settling to a particular value as empirically observed in QSL systems. These observations exclude the QSL scenario and imply that the slowly fluctuating regime is restricted to $0.2 \lesssim T/J \leqslant 1.5$, which could be due to short-range correlations.

The observed peculiar behavior prompted us to compare the structural aspects of the Yb^{3+}-based TLAFMs. The ratio of interlayer spacing to intralayer spacing $d_{inter}/d_{intra} \simeq 1.17$ in $YbBO_3$ is smaller compared to $NaYb(O, S, Se)_2$ (~1.64–1.71) and $YbGaMgO_4$ (~2.4) but almost equal to $NaBaYb(BO_3)_2$ (~1.1) [60]. In $NaYb(O, S, Se)_2$, the Yb^{3+} layers follow *ABC* stacking. This staggered arrangement generates interlayer frustration which possibly forbids magnetic LRO in zero field and fosters a QSL state [25,26,28,30]. Similarly, for $YbGaMgO_4$, a large d_{inter} leads to pronounced two-dimensionality, *ABC* stacking produces interlayer frustration, and nonmagnetic Mg-Ga site mixing results in bond randomness [5]. Consequently, the dominant effect of randomness along with magnetic frustration is responsible for curbing the magnetic LRO and establishing QSL-like behavior in $YbGaMgO_4$ [5,14,16]. On the other hand, $NaBaYb(BO_3)_2$, which has *ABC* stacking, does not possess any structural disorder and undergoes a magnetic LRO at $T_N \simeq 0.4$ K [44,44,61]. Despite having the same d_{inter} to d_{intra} ratio as $NaBaYb(BO_3)_2$ and with *AAA* stacking, $YbBO_3$ manifests no magnetic LRO and exhibits an unconventional fluctuating regime.

Interestingly, the behavior of $\lambda(T)$ resembles that of the $S = \frac{3}{2}$ TLAFMs α-$HCrO_2$ and $NaCrO_2$ [8,9]. In these compounds, there exists a broad fluctuating regime with slow dynamics at low temperatures followed by the formation of a static order at very low temperatures. The λ vs T/J plot divulges the broad maximum centered at the same position ($T/J \simeq 0.6$–0.7) for both compounds, establishing that the broad dynamical regime is universal to TLAFMs. These chromates belong to the delafossite family, where the interlayer frustration due to *ABC* stacking of the magnetic layers was believed to be the main reason for this unconventional dynamics. For $YbBO_3$, $C_{mag}(T)$ and λ feature broad maxima centered around $T/J \simeq 0.7$ ($J/k_B \simeq 0.53$ K), quite similar to the chromates. However, unlike the delafossites, the Yb^{3+} layers in $YbBO_3$ are arranged in a *AAA* stacking sequence, which is expected to produce a nonfrustrated interlayer geometry and should favor magnetic LRO at a finite temperature depending on the strength of the interlayer coupling [30].

A closer inspection of the crystal structure revealed that the Yb^{3+} ions are eightfold coordinated with oxygen [six O(1) and six O(2)] atoms forming YbO_8 polyhedra [36]. The polyhedra of two adjacent layers are connected only via partially occupied O(2) and B sites which provide the interlayer interaction path. This positional disorder of O(2) and B atoms adversely affects the local environment of Yb^{3+} and may induce bond randomness, similar to $YbMgGaO_4$. Secondly, it also weakens the interlayer interaction which is responsible for the onset of three-dimensional (3D) magnetic LRO. As a consequence, the 3D magnetic LRO is prevented, rendering the spin lattice an ideal 2D system. Thus, the absence of magnetic LRO can be credited to the nonmagnetic site disorder, and the intermediate fluctuating regime with slow dynamics could be a universal feature of isotropic TLAFMs arising due to strong intralayer frustration.

V. CONCLUSION

In summary, we performed a comprehensive study of the static and dynamic properties of a new quantum magnet, $YbBO_3$, possessing an isotropic Yb^{3+} triangular lattice. The low-temperature properties are described well by $J_{eff} = \frac{1}{2}$ Kramers doublets of the Yb^{3+} ions. Neither magnetic LRO nor spin freezing is witnessed down to 20 mK, setting the lower limit of the frustration parameter f ($=|\theta_{CW}|/T_N$) $\simeq 40$, a factual hallmark of a highly frustrated magnet. The analysis of $\chi(T)$ and magnetic isotherms suggests the emergence of strong magnetic correlations below ~0.8 K. The μSR depolarization rate together with heat capacity data demonstrate an extended fluctuating regime with slow dynamics at low temperatures. This unusual dynamics and the absence of magnetic LRO are ascribed to the effects of intralayer frustration of a perfect 2D TLAFM and positional disorder, respectively. With these features, $YbBO_3$ stands out as an exception among the Yb^{3+}-based TLAFMs.

ACKNOWLEDGMENTS

We would like to acknowledge SERB, India, for financial support (Grant No. CRG/2019/000960). Part of this work is based on experiments performed at the Swiss Muon Source (SμS), Paul Scherrer Institute, Villigen, Switzerland. The project has received funding from the European Union's Horizon 2020 research and innovation program under Marie Skłodowska-Curie Grant Agreement No. 884104 (PSI-FELLOW-III-3i). We thank Robert Scheuermann for support with the HAL instrument.

[1] L. Balents, Spin liquids in frustrated magnets, Nature (London) **464**, 199 (2010); C. Broholm, R. J. Cava, S. A. Kivelson, D. G. Nocera, M. R. Norman, and T. Senthil, Quantum spin liquids, Science **367**, eaay0668 (2020).

[2] P. Anderson, Resonating valence bonds: A new kind of insulator? Mater. Res. Bull. **8**, 153 (1973).

[3] R. R. P. Singh and D. A. Huse, Three-sublattice order in triangular- and Kagomé-lattice spin-half antiferromagnets, Phys. Rev. Lett. **68**, 1766 (1992); L. Capriotti, A. E. Trumper, and S. Sorella, Long-Range Néel Order in the Triangular Heisenberg Model, *ibid.* **82**, 3899 (1999).

[4] K. Watanabe, H. Kawamura, H. Nakano, and T. Sakai, Quantum spin-liquid behavior in the spin-1/2 random Heisenberg antiferromagnet on the triangular lattice, J. Phys. Soc. Jpn. **83**, 034714 (2014).

[5] I. Kimchi, A. Nahum, and T. Senthil, Valence Bonds in Random Quantum Magnets: Theory and Application to $YbMgGaO_4$, Phys. Rev. X **8**, 031028 (2018).

[6] P. H. Y. Li, R. F. Bishop, and C. E. Campbell, Quasiclassical magnetic order and its loss in a spin-$\frac{1}{2}$ Heisenberg antiferromagnet on a triangular lattice with competing bonds, Phys. Rev. B **91**, 014426 (2015).

[7] P. A. Maksimov, Z. Zhu, S. R. White, and A. L. Chernyshev, Anisotropic-Exchange Magnets on a Triangular Lattice: Spin Waves, Accidental Degeneracies, and Dual Spin Liquids, Phys. Rev. X **9**, 021017 (2019).

[8] K. Somesh, Y. Furukawa, G. Simutis, F. Bert, M. Prinz-Zwick, N. Büttgen, A. Zorko, A. A. Tsirlin, P. Mendels, and R. Nath, Universal fluctuating regime in triangular chromate antiferromagnets, Phys. Rev. B **104**, 104422 (2021).

[9] A. Olariu, P. Mendels, F. Bert, B. G. Ueland, P. Schiffer, R. F. Berger, and R. J. Cava, Unconventional Dynamics in Triangular Heisenberg Antiferromagnet $NaCrO_2$, Phys. Rev. Lett. **97**, 167203 (2006).

[10] R. Kaneko, S. Morita, and M. Imada, Gapless spin-liquid phase in an extended spin 1/2 triangular Heisenberg model, J. Phys. Soc. Jpn. **83**, 093707 (2014).

[11] Y. Li, P. Gegenwart, and A. A. Tsirlin, Spin liquids in geometrically perfect triangular antiferromagnets, J. Phys.: Condens. Matter **32**, 224004 (2020).

[12] Y. D. Li, X. Wang, and G. Chen, Anisotropic spin model of strong spin-orbit-coupled triangular antiferromagnets, Phys. Rev. B **94**, 035107 (2016).

[13] T. Furukawa, K. Miyagawa, T. Itou, M. Ito, H. Taniguchi, M. Saito, S. Iguchi, T. Sasaki, and K. Kanoda, Quantum Spin Liquid Emerging from Antiferromagnetic Order by Introducing Disorder, Phys. Rev. Lett. **115**, 077001 (2015).

[14] Y. Li, G. Chen, W. Tong, L. Pi, J. Liu, Z. Yang, X. Wang, and Q. Zhang, Rare-Earth Triangular Lattice Spin Liquid: A Single-Crystal Study of $YbMgGaO_4$, Phys. Rev. Lett. **115**, 167203 (2015).

[15] Y. Li, H. Liao, Z. Zhang, S. Li, F. Jin, L. Ling, L. Zhang, Y. Zou, L. Pi, Z. Yang, J. Wang, Z. Wu, and Q. Zhang, Gapless quantum spin liquid ground state in the two-dimensional spin-1/2 triangular antiferromagnet $YbMgGaO_4$, Sci. Rep. **5**, 16419 (2015).

[16] Y. Li, D. Adroja, R. I. Bewley, D. Voneshen, A. A. Tsirlin, P. Gegenwart, and Q. Zhang, Crystalline Electric-Field Randomness in the Triangular Lattice Spin-Liquid $YbMgGaO_4$, Phys. Rev. Lett. **118**, 107202 (2017).

[17] Z. Zhu, P. A. Maksimov, S. R. White, and A. L. Chernyshev, Disorder-Induced Mimicry of a Spin Liquid in $YbMgGaO_4$, Phys. Rev. Lett. **119**, 157201 (2017).

[18] X. Zhang, F. Mahmood, M. Daum, Z. Dun, J. A. M. Paddison, N. J. Laurita, T. Hong, H. Zhou, N. P. Armitage, and M. Mourigal, Hierarchy of Exchange Interactions in the Triangular-Lattice Spin Liquid $YbMgGaO_4$, Phys. Rev. X **8**, 031001 (2018).

[19] Z. Ma, J. Wang, Z.-Y. Dong, J. Zhang, S. Li, S.-H. Zheng, Y. Yu, W. Wang, L. Che, K. Ran, S. Bao, Z. Cai, P. Čermák, A. Schneidewind, S. Yano, J. S. Gardner, X. Lu, S.-L. Yu, J.-M. Liu, S. Li *et al.*, Spin-Glass Ground State in a Triangular-Lattice Compound $YbZnGaO_4$, Phys. Rev. Lett. **120**, 087201 (2018).

[20] L. Liu, H. Shao, Y.-C. Lin, W. Guo, and A. W. Sandvik, Random-Singlet Phase in Disordered Two-Dimensional Quantum Magnets, Phys. Rev. X **8**, 041040 (2018).

[21] Z. Ma, Z.-Y. Dong, J. Wang, S. Zheng, K. Ran, S. Bao, Z. Cai, Y. Shangguan, W. Wang, M. Boehm, P. Steffens, L.-P. Regnault, X. Wang, Y. Su, S.-L. Yu, J.-M. Liu, J.-X. Li, and J. Wen, Disorder-induced broadening of the spin waves in the triangular-lattice quantum spin liquid candidate $YbZnGaO_4$, Phys. Rev. B **104**, 224433 (2021).

[22] J. A. M. Paddison, M. Daum, Z. Dun, G. Ehlers, Y. Liu, M. B. Stone, H. Zhou, and M. Mourigal, Continuous excitations of the triangular-lattice quantum spin liquid $YbMgGaO_4$, Nat. Phys. **13**, 117 (2017).

[23] Y. Li, D. Adroja, P. K. Biswas, P. J. Baker, Q. Zhang, J. Liu, A. A. Tsirlin, P. Gegenwart, and Q. Zhang, Muon Spin Relaxation Evidence for the U(1) Quantum Spin-Liquid Ground State in the Triangular Antiferromagnet $YbMgGaO_4$, Phys. Rev. Lett. **117**, 097201 (2016).

[24] B. Schmidt, J. Sichelschmidt, K. M. Ranjith, T. Doert, and M. Baenitz, Yb delafossites: Unique exchange frustration of $4f$ spin-$\frac{1}{2}$ moments on a perfect triangular lattice, Phys. Rev. B **103**, 214445 (2021).

[25] M. Baenitz, P. Schlender, J. Sichelschmidt, Y. A. Onykiienko, Z. Zangeneh, K. M. Ranjith, R. Sarkar, L. Hozoi, H. C. Walker, J.-C. Orain, H. Yasuoka, J. van den Brink, H. H. Klauss, D. S. Inosov, and T. Doert, $NaYbS_2$: A planar spin-$\frac{1}{2}$ triangular-lattice magnet and putative spin liquid, Phys. Rev. B **98**, 220409(R) (2018).

[26] K. M. Ranjith, D. Dmytriieva, S. Khim, J. Sichelschmidt, S. Luther, D. Ehlers, H. Yasuoka, J. Wosnitza, A. A. Tsirlin, H. Kühne, and M. Baenitz, Field-induced instability of the quantum spin liquid ground state in the $J_{\text{eff}} = \frac{1}{2}$ triangular-lattice compound $NaYbO_2$, Phys. Rev. B **99**, 180401(R) (2019).

[27] M. M. Bordelon, E. Kenney, C. Liu, T. Hogan, L. Posthuma, M. Kavand, Y. Lyu, M. Sherwin, N. P. Butch, C. Brown, M. J. Graf, L. Balents, and S. D. Wilson, Field-tunable quantum disordered ground state in the triangular-lattice antiferromagnet $NaYbO_2$, Nat. Phys. **15**, 1058 (2019); L. Ding, P. Manuel, S. Bachus, F. Grußler, P. Gegenwart, J. Singleton, R. D. Johnson, H. C. Walker, D. T. Adroja, A. D. Hillier, and A. A. Tsirlin, Gapless spin-liquid state in the structurally disorder-free triangular antiferromagnet $NaYbO_2$, Phys. Rev. B **100**, 144432 (2019).

[28] K. M. Ranjith, S. Luther, T. Reimann, B. Schmidt, P. Schlender, J. Sichelschmidt, H. Yasuoka, A. M. Strydom, Y. Skourski, J. Wosnitza, H. Kühne, T. Doert, and M. Baenitz, Anisotropic field-induced ordering in the triangular-lattice quantum spin liquid $NaYbSe_2$, Phys. Rev. B **100**, 224417 (2019).

[29] J. Guo, X. Zhao, S. Ohira-Kawamura, L. Ling, J. Wang, L. He, K. Nakajima, B. Li, and Z. Zhang, Magnetic-field and composition tuned antiferromagnetic instability in the quantum spin-liquid candidate $NaYbO_2$, Phys. Rev. Mater. **4**, 064410 (2020).

[30] M. M. Bordelon, C. Liu, L. Posthuma, P. M. Sarte, N. P. Butch, D. M. Pajerowski, A. Banerjee, L. Balents, and S. D. Wilson, Spin excitations in the frustrated triangular lattice antiferromagnet $NaYbO_2$, Phys. Rev. B **101**, 224427 (2020).

[31] Z. Zhang, J. Li, M. Xie, W. Zhuo, D. T. Adroja, P. J. Baker, T. G. Perring, A. Zhang, F. Jin, J. Ji, X. Wang, J. Ma, and Q. Zhang, Low-energy spin dynamics of the quantum spin liquid candidate $NaYbSe_2$, Phys. Rev. B **106**, 085115 (2022); P.-L. Dai, G. Zhang, Y. Xie, C. Duan, Y. Gao, Z. Zhu, E. Feng, Z. Tao, C.-L. Huang, H. Cao, A. Podlesnyak, G. E. Granroth, M. S. Everett, J. C. Neuefeind, D. Voneshen, S. Wang, G. Tan, E. Morosan, X. Wang, H.-Q. Lin *et al.*, Spinon Fermi Surface Spin Liquid in a Triangular Lattice Antiferromagnet $NaYbSe_2$, Phys. Rev. X **11**, 021044 (2021).

[32] R. Sarkar, P. Schlender, V. Grinenko, E. Haeussler, P. J. Baker, T. Doert, and H.-H. Klauss, Quantum spin liquid ground state in the disorder free triangular lattice $NaYbS_2$, Phys. Rev. B **100**, 241116(R) (2019).

[33] K. Y. Zeng, L. Ma, Y. X. Gao, Z. M. Tian, L. S. Ling, and L. Pi, NMR study of the spin excitations in the frustrated antiferromagnet $Yb(BaBO_3)_3$ with a triangular lattice, Phys. Rev. B **102**, 045149 (2020).

[34] R. Bag, M. Ennis, C. Liu, S. E. Dissanayake, Z. Shi, J. Liu, L. Balents, and S. Haravifard, Realization of quantum dipoles in triangular lattice crystal $Ba_3Yb(BO_3)_3$, Phys. Rev. B **104**, L220403 (2021).

[35] Y. Tokiwa, S. Bachus, K. Kavita, A. Jesche, A. A. Tsirlin, and P. Gegenwart, Frustrated magnet for adiabatic demagnetization cooling to milli-Kelvin temperatures, Commun. Mater. **2**, 42 (2021).

[36] G. Chadeyron, M. El-Ghozzi, R. Mahiou, A. Arbus, and J. Cousseins, Revised structure of the orthoborate YBO_3, J. Solid State Chem. **128**, 261 (1997).

[37] S. Hosokawa, Y. Tanaka, S. Iwamoto, and M. Inoue, Morphology and structure of rare earth borate ($RE BO_3$) synthesized by glycothermal reaction, J. Mater. Sci **43**, 2276 (2008).

[38] D. Rauch, M. Kraken, F. J. Litterst, S. Süllow, H. Luetkens, M. Brando, T. Förster, J. Sichelschmidt, A. Neubauer, C. Pfleiderer, W. J. Duncan, and F. M. Grosche, Spectroscopic study of metallic magnetism in single-crystalline $Nb_{1-y}Fe_{2+y}$, Phys. Rev. B **91**, 174404 (2015).

[39] A. Abragam and B. Bleaney, *Electron Paramagnetic Resonance of Transition Ions* (Oxford University Press, Oxford, 2012).

[40] A. Amato, H. Luetkens, K. Sedlak, A. Stoykov, R. Scheuermann, M. Elender, A. Raselli, and D. Graf, The new versatile general purpose surface-muon instrument (GPS) based on silicon photomultipliers for μ^+SR measurements on a continuous-wave beam, Rev. Sci. Instrum. **88**, 093301 (2017).

[41] R. C. Juan, Recent advances in magnetic structure determination by neutron powder diffraction, Physica B: Condensed Matter **192**, 55 (1993).

[42] S. S. Islam, K. M. Ranjith, M. Baenitz, Y. Skourski, A. A. Tsirlin, and R. Nath, Frustration of square cupola in $Sr(TiO)Cu_4(PO_4)_4$, Phys. Rev. B **97**, 174432 (2018).

[43] K. M. Ranjith, K. Brinda, U. Arjun, N. G. Hegde, and R. Nath, Double phase transition in the triangular antiferromagnet $Ba_3CoTa_2O_9$, J. Phys.: Condens. Matter **29**, 115804 (2017).

[44] S. Guo, A. Ghasemi, C. L. Broholm, and R. J. Cava, Magnetism on ideal triangular lattices in $NaBaYb(BO_3)_2$, Phys. Rev. Mater. **3**, 094404 (2019).

[45] R. Sibille, E. Lhotel, V. Pomjakushin, C. Baines, T. Fennell, and M. Kenzelmann, Candidate Quantum Spin Liquid in the Ce^{3+} Pyrochlore Stannate $Ce_2Sn_2O_7$, Phys. Rev. Lett. **115**, 097202 (2015).

[46] Y. Savina, O. Bludov, V. Pashchenko, S. L. Gnatchenko, P. Lemmens, and H. Berger, Magnetic properties of the antiferromagnetic spin-$\frac{1}{2}$ chain system β-$TeVO_4$, Phys. Rev. B **84**, 104447 (2011); P. K. Mukharjee, K. Somesh, K. M. Ranjith, M. Baenitz, Y. Skourski, D. T. Adroja, D. Khalyavin, A. A. Tsirlin, and R. Nath, Quantum magnetism of ferromagnetic spin dimers in $\alpha - KVOPO_4$, *ibid.* **104**, 224409 (2021).

[47] C. Kittel, *Introduction to Solid State Physics* (Wiley, Hoboken, NJ, 2005).

[48] R. Orbach and B. Bleaney, Spin-lattice relaxation in rare-earth salts, Proc. Math. Phys. Eng. Sci. **264**, 458 (1961).

[49] S. Kundu, A. Hossain, Pranava Keerthi S, R. Das, M. Baenitz, P. J. Baker, J.-C. Orain, D. C. Joshi, R. Mathieu, P. Mahadevan, S. Pujari, S. Bhattacharjee, A. V. Mahajan, and D. D. Sarma, Signatures of a Spin-$\frac{1}{2}$ Cooperative Paramagnet in the Diluted Triangular Lattice of Y_2CuTiO_6, Phys. Rev. Lett. **125**, 117206 (2020).

[50] B. Bernu and G. Misguich, Specific heat and high-temperature series of lattice models: Interpolation scheme and examples on quantum spin systems in one and two dimensions, Phys. Rev. B **63**, 134409 (2001).

[51] M. S. Makivić and H.-Q. Ding, Two-dimensional spin-1/2 Heisenberg antiferromagnet: A quantum Monte Carlo study, Phys. Rev. B **43**, 3562 (1991); J.-K. Kim and M. Troyer, Low Temperature Behavior and Crossovers of the Square Lattice Quantum Heisenberg Antiferromagnet, Phys. Rev. Lett. **80**, 2705 (1998).

[52] *Strongly Correlated Systems: Numerical Methods*, edited by A. Avella and F. Mancini, Springer Series in Solid-State Sciences Vol. 176 (Springer, Berlin, 2013).

[53] S. Lee, R. Klauer, J. Menten, W. Lee, S. Yoon, H. Luetkens, P. Lemmens, A. Möller, and K.-Y. Choi, Unconventional spin excitations in the $S = \frac{3}{2}$ triangular antiferromagnet $RbAg_2Cr[VO_4]_2$, Phys. Rev. B **101**, 224420 (2020).

[54] Y. J. Uemura, A. Keren, K. Kojima, L. P. Le, G. M. Luke, W. D. Wu, Y. Ajiro, T. Asano, Y. Kuriyama, M. Mekata, H. Kikuchi, and K. Kakurai, Spin Fluctuations in Frustrated Kagomé Lattice System $SrCr_8Ga_4O_{19}$ Studied by Muon Spin Relaxation, Phys. Rev. Lett. **73**, 3306 (1994).

[55] S. Lee, C. H. Lee, A. Berlie, A. D. Hillier, D. T. Adroja, R. Zhong, R. J. Cava, Z. H. Jang, and K.-Y. Choi, Temporal and field evolution of spin excitations in the disorder-free triangular antiferromagnet $Na_2BaCo(PO_4)_2$ Phys. Rev. B **103**, 024413 (2021).

[56] A. Keren, P. Mendels, I. A. Campbell, and J. Lord, Probing the Spin-Spin Dynamical Autocorrelation Function in a Spin Glass above T_g via Muon Spin Relaxation, Phys. Rev. Lett. **77**, 1386 (1996).

[57] N. Onishi, K. Oka, M. Azuma, Y. Shimakawa, Y. Motome, T. Taniguchi, M. Hiraishi, M. Miyazaki, T. Masuda,

A. Koda, K. M. Kojima, and R. Kadono, Magnetic ground state of the frustrated honeycomb lattice antiferromagnet $Bi_3Mn_4O_{12}(NO_3)$, Phys. Rev. B **85**, 184412 (2012).

[58] I. A. Campbell, A. Amato, F. N. Gygax, D. Herlach, A. Schenck, R. Cywinski, and S. H. Kilcoyne, Dynamics in canonical spin glasses observed by muon spin depolarization, Phys. Rev. Lett. **72**, 1291 (1994).

[59] P. Mendels, F. Bert, M. A. de Vries, A. Olariu, A. Harrison, F. Duc, J. C. Trombe, J. S. Lord, A. Amato, and C. Baines, Quantum Magnetism in the Paratacamite Family: Towards an Ideal Kagomé Lattice, Phys. Rev. Lett. **98**, 077204 (2007).

[60] S. Guo, R. Zhong, K. Górnicka, T. Klimczuk, and R. J. Cava, Crystal growth, structure, and magnetism of the 2D spin 1/2 triangular lattice material $Rb_3Yb(PO_4)_2$, Chem. Mater. **32**, 10670 (2020).

[61] B. L. Pan, J. M. Ni, L. P. He, Y. J. Yu, Y. Xu, and S. Y. Li, Specific heat and thermal conductivity of the triangular-lattice rare-earth material $KBaYb(BO_3)_2$ at ultralow temperature, Phys. Rev. B **103**, 104412 (2021).